Journal of Sol-Gel Science and Technology (2025) 114:762–777
https://doi.org/10.1007/s10971-025-06739-z

ORIGINAL PAPER

Tailoring the physical properties of ultrasonically spray pyrolyzed SnS thin films with silver doping

Ibrahim Gunes[1,2] · Emrah Sarica[3] · Vildan Bilgin[4] · Ayse Kucukarslan[4]

Received: 12 September 2024 / Accepted: 17 March 2025 / Published online: 27 March 2025

Abstract

In this study, the effects of silver (Ag) doping on the structural, morphological, optical, and electrical properties of tin monosulfide (SnS) thin films were investigated. The films, undoped and doped with 3%, 6%, and 9% Ag, were deposited using the ultrasonic spray pyrolysis (USP) technique at a substrate temperature of 350 °C. X-ray diffraction (XRD) analysis confirmed a π-SnS (cubic) structure with (400) preferred orientation for undoped and ≤ 6% Ag-doped films, while 9% doping induced amorphization due to severe lattice distortions. Morphological analyses revealed smooth, void-free surfaces, with average roughness increasing from 5.8 nm (undoped) to 19.6 nm (9% doping). Optical measurements showed that the band gap widened from 1.84 eV (undoped) to 2.47 eV (9% Ag-doped), and Urbach energy increased from 190 meV to 600 meV. Hall effect measurements confirmed p-type conductivity for all films. Resistivity ranged from 4.34×10^5 Ωcm to 9.48×10^5 Ωcm, carrier concentration varied between 2.7×10^{12} cm^{-3} and 5.6×10^{12} cm^{-3}, while mobility decreased from 3.3×10^1 cm^2/Vs to 2.0×10^1 cm^2/Vs with increasing Ag doping. These findings demonstrate that Ag doping significantly influences the structural and optoelectronic behavior of SnS thin films, making them promising candidates for thin-film solar cells and optoelectronic applications.

Graphical Abstract

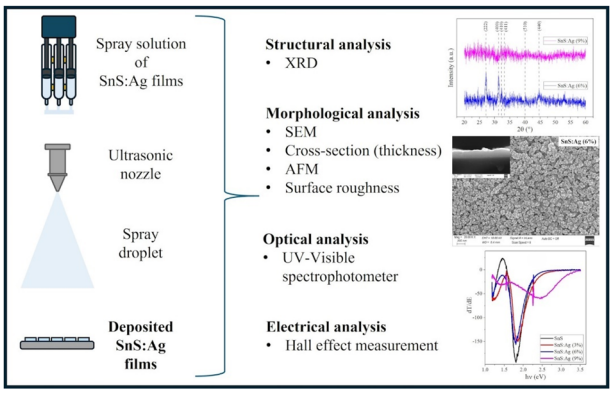

Keywords Ultrasonic spray pyrolysis · SnS:Ag thin films · Absorber layer · Thin film solar cells.

✉ Ibrahim Gunes
ibrahimgunes@comu.edu.tr

[1] Department of Energy Management, Canakkale Faculty of Applied Sciences, Çanakkale Onsekiz Mart University, Çanakkale, Turkey

[2] Department of Electricity and Energy, Biga Vocational School, Çanakkale Onsekiz Mart University, Çanakkale, Turkey

[3] Department of Electrical and Electronics Engineering, Faculty of Engineering, Baskent University, Ankara, Turkey

[4] Department of Physics, Faculty of Sciences, Çanakkale Onsekiz Mart University, Çanakkale, Turkey

Highlights

- Ag doping narrows crystallite size; 9% doping results in amorphous SnS films.
- Optical band gap widens from 1.83 eV to 2.47 eV with increased Ag doping.
- SEM/AFM reveal nearly void-free surfaces; roughness increases with Ag doping.
- High Urbach energy signals increased electronic disorder with higher Ag doping.
- Ag doping optimizes SnS films for photovoltaic and optoelectronic applications.

1 Introduction

Nowadays, new material discoveries come to the fore in order to develop sustainable and environmentally friendly technologies and increase energy efficiency [1]. Thin film solar cells (TFSCs) attract attention with their lower cost advantage and competitive conversion efficiencies compared to silicon-based solar cells [2]. In particular, $Cu(In,Ga)(S,Se)_2$ (CIGS) and CdTe based solar cells hold an important place in the market with conversion efficiencies exceeding 22% [2, 3]. However, the scarcity of toxic substances such as Cd and critical raw materials such as In, Ga, and Te contained in these technologies direct researchers to conduct research on more environmentally friendly and widely available alternative materials such as $Cu_2ZnSn(S,Se)_4$ (CZTS) [4, 5]. Nevertheless, the complex structural features of CZTS and the formation of undesirable secondary phases prevent this material from achieving high efficiency in solar cells [5, 6]. Therefore, this has prompted a growing interest in simple binary compound materials, which are low-cost and composed of earth-abundant elements.

Tin monosulfide (SnS) is considered a promising material for optoelectronic applications due to its exceptional properties, such as a high absorption coefficient ($> 10^4\ cm^{-1}$) and a suitable direct band gap (1.3 eV to 1.8 eV) [7–11]. Furthermore, SnS is non-toxic, environmentally friendly, and composed of earth-abundant elements, aligning with global efforts toward sustainable energy solutions [12, 13]. However, despite theoretical predictions indicating that SnS-based thin films could achieve efficiencies of up to 24%, their practical application has so far yielded efficiencies below 4%, with only a few studies reporting slightly higher values [10, 14–19]. The main obstacles to achieving higher efficiencies include difficulties in producing high-quality material, selecting appropriate buffer layers, minimizing interface losses, and the formation of undesirable phases [13, 20, 21]. On the other hand, SnS can crystallize in two primary phases: orthorhombic and cubic [22]. The orthorhombic phase (α-SnS) is the thermodynamically stable form under standard conditions, with a layered structure that gives rise to anisotropic optical and electrical properties [23]. It typically exhibits a direct band gap of 1.3 eV [24, 25], making it ideal for photovoltaic applications. However, its anisotropic nature can hinder charge transport, limiting its efficiency [26]. In contrast, the cubic phase (π-SnS) offers more symmetric, isotropic properties [27]. It can be stabilized through certain deposition techniques or doping processes and typically shows a wider band gap (up to 1.7 eV), making it suitable for applications where higher energy absorption or tunable optical properties are required [28]. Moreover, π-SnS demonstrates excellent structural stability at room temperature, which, combined with its isotropic optical properties, makes it highly valuable for photovoltaic and optoelectronic applications [29, 30]. In comparison to its orthorhombic phase, the cubic phase may offer better carrier mobility, which enhances charge transport [27, 31]. This feature is advantageous for both photovoltaic devices and other optoelectronic systems, improving efficiency and device performance [27, 31, 32]. Although deposition and doping processes have been explored to stabilize the cubic phase of SnS by tuning its structural properties, studies on cubic SnS remain limited, posing challenges in fully understanding its behavior and ensuring consistent performance for photovoltaic and optoelectronic applications.

External doping is widely preferred to enhance the physical properties of semiconductors, and similar strategies have been applied to SnS to improve its performance. Recent studies have indicated that doping SnS films with elements such as bismuth (Bi) [33], cadmium (Cd) [34], copper (Cu) [35], nickel (Ni) [36], selenium (Se) [37], silver (Ag) [38], indium (In) [39], iron (Fe) [40] and neodymium (Nd) [41] significantly alters their optoelectronic behavior. By incorporating external dopants, it is possible to adjust the electrical conductivity, carrier concentration, and optical properties of SnS, making it more suitable not only for photovoltaic devices but also for other optoelectronic applications. Research indicates that the cubic π-SnS phase is well-suited for optoelectronic applications, including thermoelectric devices and near-infrared (NIR) photodetectors [42, 43]. Its advantageous band structure and high absorption across the NIR-visible spectrum make it promising for energy conversion and sensing technologies [44]. π-SnS structural stability and tunable properties further enhance its potential for efficient light harvesting and thermoelectric performance [42–45]. For example, it has been suggested that the band gap of 3% Bi-doped

orthorhombic SnS films deposited by thermal evaporation technique decreases with doping (from 1.85 eV to 1.6 eV) and is suitable for photovoltaic performance by improving their optical properties [33]. In another study, orthorhombic SnS films doped with various concentrations (0%, 0.5%, 1%, 1.5%, and 2%) of Cd deposited via the sol-gel technique clearly showed improvements in crystallinity, electrical properties, and photovoltaic efficiency [34]. It was reported that films with 1.5% Cd doping exhibited the highest efficiency, achieving a 61% higher efficiency compared to undoped films, with a maximum efficiency of 1.34% [34]. It has also been reported that Cu-doped SnS films deposited at different rates (0%, 2%, 5% and 10%) by ultrasonic spray pyrolysis technique change the crystal structure (undoped= cubic, doped= orthorhombic) and optical properties with increasing carrier concentration and carrier mobility [35]. In the same study, it was reported that a 5% doped SnS:Cu absorber layer could reach an efficiency of 6.27%, through simulation based on the collected experimental data [35]. In another study, it was suggested that Ni-doped SnS films deposited by chemical bath deposition technique reduced the resistivity (0.42×10^5 Ωcm) at 6% doping, making them promising for optoelectronic applications [36]. In another study, it was reported that $SnS_{1-x}Se_x$ ($x = 0$, 0.1, 0.15, 0.2, 0.25) films deposited by thermal evaporation technique increased the crystallinity level, decreased permeability, increased absorption and narrowed the optical band gap as the Se concentration increased [37]. Accordingly, in the same study, it was suggested that the findings obtained could be made suitable for TFSCs and thermal applications by adjusting the Se concentration [37]. In contrast to these studies focusing on other dopants, several investigations have explored the effects of Ag doping on the optoelectronic properties of SnS thin films. However, these works have primarily concentrated on orthorhombic phase SnS. For instance, Ag-doped SnS thin films at different rates (0%, 2%, 4% and 6%) deposited by thermal evaporation crystallize in the orthorhombic phase [38]. As doping concentration increase, the absorption coefficients improve ($> 10^4$ cm^{-1}), and the optical band gap narrows (from 2.6 eV to 1.7 eV) [38]. In the same study, *p*-SnS/*n*-Si heterostructures were created, and the highest photovoltaic efficiency of 5.4% was reported with 6% Ag doping [38]. Ag is chosen as a dopant for SnS due to its ability to enhance electrical conductivity, increase carrier concentration, and improve thermoelectric performance by introducing holes into the material [46–50]. Ag effectively shifts the Fermi level towards the valence band, which enhances the p-type behavior of SnS and boosts charge transport properties [46, 51]. This makes Ag-doped SnS an attractive option for both thermoelectric and optoelectronic applications, such as photovoltaics and photodetectors. Additionally, Ag doping reduces thermal conductivity, further increasing the material's efficiency in energy applications [47, 49]. However, precise control over Ag concentration is required to avoid excessive defects that could impair performance [45, 47]. Research suggests that precise control over Ag concentration is crucial to balancing conductivity and maintaining structural stability in SnS-based devices. However, research on Ag doping in cubic-phase SnS remains limited, despite its potential for various optoelectronic applications beyond photovoltaics.

Undoped and doped SnS thin films can be produced using various techniques such as thermal evaporation [8, 52], atomic layer deposition (ALD) [53–55], RF sputtering [35, 56, 57], chemical vapor deposition (CVD) [28, 58], spin coating [59, 60], electrochemical deposition [39, 61], and spray pyrolysis [41, 62, 63] as documented in the literature. Among these, ultrasonic spray pyrolysis (USP) offers several distinct advantages: it allows for large-area film deposition, is cost-effective compared to techniques like ALD, and enables precise control of dopant concentrations, ensuring uniform film growth [64–66]. These advantages make USP an attractive technique not only for photovoltaic applications but also for other optoelectronic devices. In this context, this study investigates the effect of Ag doping on the structural, morphological, optical and electrical properties of cubic SnS thin films deposited via ultrasonic spray pyrolysis (USP). In contrast to the widely studied orthorhombic SnS phase, research on Ag-doped cubic SnS remains rather limited and is one of the few studies in the literature that examines this topic. This study systematically examines the effect of Ag doping, contributing to the growing body of research in the field and providing valuable information on doping mechanisms and optoelectronic behavior. However, optimizing the deposition parameters for improved device performance remains a subject of future research. The findings provide important insights into the incorporation of Ag into cubic SnS films, supporting their potential use in thin-film solar cells and other optoelectronic applications.

2 Experimental methods

2.1 Deposition of SnS and SnS:Ag thin films

Undoped and Ag-doped SnS thin films at different rates (3%, 6%, 9%) were deposited on glass substrates using the ultrasonic spray pyrolysis (USP) technique at a substrate temperature of 350 °C. The schematic diagram of the thin film deposited system can be found in our prior publication [67]. To prepare the spray solutions, 0.05 M tin (II) chloride dihydrate ($SnCl_2.2H_2O$; ≥ 98.0%, Merck, Darmstadt, Germany), 0.075 M thiourea (CH_4N_2S; ≥99.0%, Sigma-

Aldrich, St. Louis, USA), and 0.05 M silver nitrate ($AgNO_3$; ≥99.9%, Merck, Darmstadt, Germany) salts were used, and deionized (DI) water was used as the solvent. However, to prevent the precipitation of $SnCl_2.2H_2O$ in DI water, the tin salt was initially dissolved in 5 mL of hydrochloric acid (HCI) at 60 °C. The solution was then diluted with 95 mL of DI water, resulting in the desired HCI:DI (5:95) volume ratio. This adjustment ensured the stability of the spray solution. Moreover, the sulfur concentration was selected higher than the tin concentration to minimize sulfur losses during deposition, which is essential to maintaining stoichiometry and preventing defect formation. On the other hand, the spray solution concentrations and dopant rates were selected based on preliminary trials and aligned with similar approaches reported in the literature, ensuring well-dissolved solutions, uniform films, and reasonable structural stability, although variations in electrical and optical properties were observed. Before deposition, the glass substrates (~ 1 × 1 cm and ~1 × 2 cm) were first cut to size, then cleaned in a detergent + DI water mixture for 15 min, followed by ultrasonic cleaning in DI water for another 15 min. After drying with filter paper, the substrates were carefully placed on the heating surface, ready for deposition. The spray solution was applied for 30 min using 1 bar of compressed air, with a solution flow rate of 5 ml/min. After deposition, the films were left to cool naturally in the spray chamber. Since silver is prone to oxidation, special care was taken to store the films. After deposition, the films were placed in sample containers, sealed with parafilm to limit exposure to air, and stored at room temperature in a dry oven to prevent oxidation. After the deposition process was completed, the characterization stage was performed to analyze the structural, morphological, optical, and electrical properties of the films.

2.2 Characterization of SnS and SnS:Ag thin films

Structural analyses were evaluated using the PANalytical Empyrean X-ray diffraction (XRD) device. Using CuK_α radiation ($\lambda = 1.5405$ Å) at 45 kV/30 mA, XRD patterns were obtained in continuous scanning mode with a step size of 0.013° in the 2θ range between 20° and 60°. Surface morphology and film thicknesses were examined using a Carl Zeiss-Gemini 300 scanning electron microscope (SEM). Surface topology and roughness values were analyzed using a Park Systems XE 100 atomic force microscope (AFM) operated in non-contact mode at room temperature. Optical properties of the films were performed using a Rigol Ultra-3660 double-beam UV-Visible spectrophotometer. Electrical properties were evaluated using the Ecopia HMS-3000 Hall Effect Measurement System. Gold contacts were applied to thin films with dimensions of 1 × 1 cm using the Van der Pauw method at room temperature. With this comprehensive characterization process, the effect of Ag doping on the structural, morphological, optical, and electrical properties of SnS films was evaluated.

3 Results and discussions

3.1 XRD analysis

Figure 1a shows the XRD scan of SnS thin films over a wide diffraction angle range (20°-60°), providing an overview of the crystalline phases. However, Fig. 1b focuses on a narrower diffraction angle range (25°-35°) to examine peak shifts and broadening more precisely. In this study, the diffraction patterns obtained were compared with the reference JCPDS (Joint Committee on Powder Diffraction Standards) cards, and the Miller indices and the crystal systems to which the peaks observed on the patterns belong were identified. The XRD patterns shown in Fig. 1a were matched with the α-SnS phase (JCPDS card no. 39-0354) and the π-SnS phase (JCPDS card no. 86-9477), introduced in 2017 [22, 67–69]. These patterns, differing from the α-SnS crystal structure, matched the π-SnS crystal structure. The triple peak structure observed especially in the 30°-33° range is a characteristic feature of the cubic phase, as previously reported in the literature [67–69]. This distinctive peak arrangement provides strong evidence for the presence of a cubic SnS phase in the deposited films. It was also identified by peaks corresponding to the Miller indices (222), (400), (410), (411), (510), (440), and (622). The positions and intensities of these peaks provide critical information about the crystal structure and possible phase transformations in the films. Therefore, in the diffraction patterns seen in Fig. 1a, the presence of possible secondary phases such as SnS_2 (JCPDS card no. 23-0677), Sn_2S_3 (JCPDS card no. 14-0619) and SnO_2 (JCPDS no. 41-1445) was examined by comparing with the relevant JCPDS cards. In this context, SnS_2 or Sn_2S_3 phases were not detected in the XRD patterns. However, the reference pattern for the SnO_2 phase shows a peak at approximately 2θ~27°, which coincides with the dominant π-SnS peak (Fig. 2b). Due to this overlap and the limitations of XRD in detecting low-concentration phases, the presence of SnO_2 cannot be confirmed definitively. Additional characterization, such as Raman spectroscopy, would be required for conclusive identification. As is known, the overlapping of peaks of different phases in XRD patterns and the high signal-to-noise ratio are common phenomena that make it difficult to detect low-concentration phases. Unfortunately, Raman analysis could not be performed in this study due to infrastructure constraints. However, various studies have reported that the deposition process of SnS films under open-air

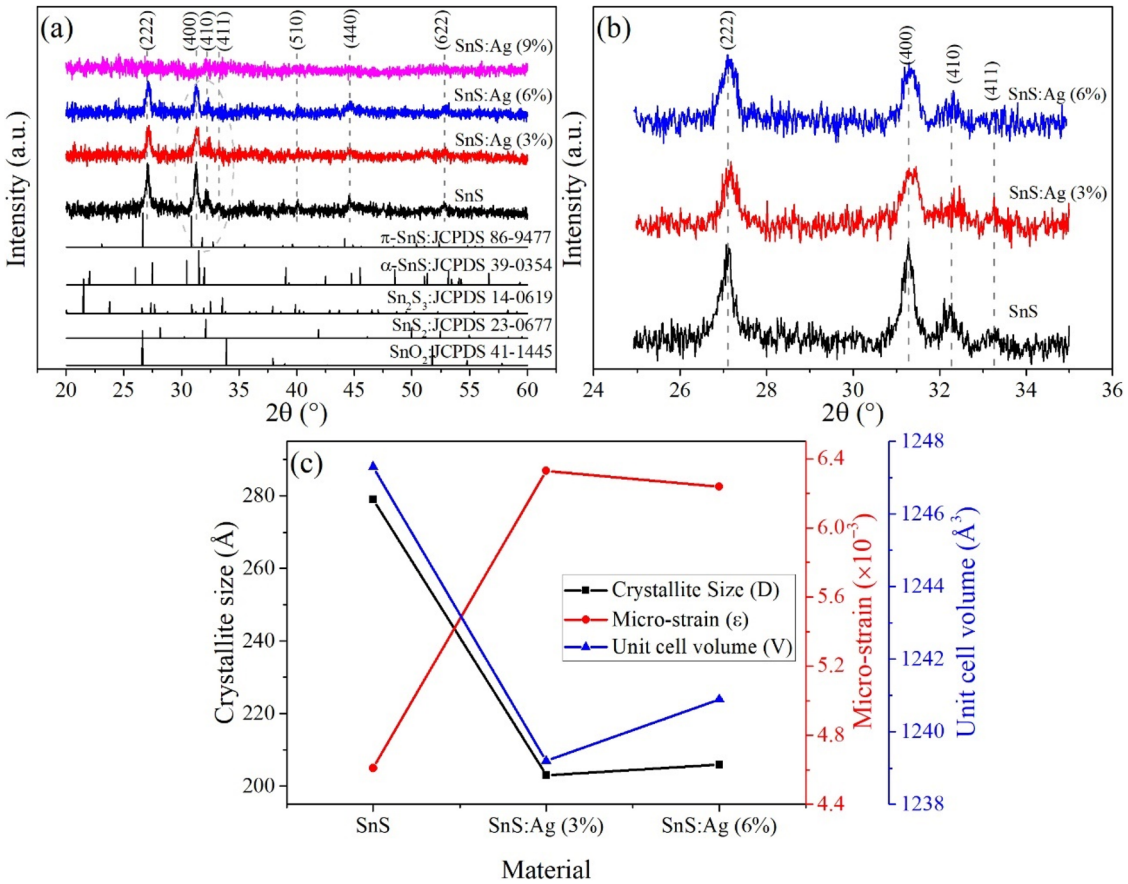

Fig. 1 **a** XRD patterns of SnS:Ag (0%, 3%, 6%, and 9%) thin films over a wide diffraction angle range (20°–60°), providing an overview of the crystalline phases, (**b**) XRD patterns of SnS:Ag (0%, 3%, 6%, and 9%) thin films over a narrower diffraction angle range (25°–35°), highlighting peak shifts and broadening, and (**c**). The relationship between crystallite size (*D*), micro-strain (*ε*), and unit cell volume (*V*) for SnS:Ag (0%, 3%, 6%, and 9%) thin films

conditions can lead to the formation of oxide phases such as Sn_xO_y (SnO_2), and that substrate temperature, along with other impurity phases, is one of the key factors affecting this formation. Polivtseva et al. [70] reported in their study on films deposited by spray method that SnS_2, Sn_2S_3, and SnO_2 phases were not observed at temperatures below 320 °C, but orthorhombic SnS phase was dominant. On the other hand, it was reported that SnS phase was not observed and SnS_2 and SnO_2 phases were detected at substrate temperatures above 370 °C [70]. In another study conducted by spray method, it was stated that Sn_2S_3 phase was dominant in films deposited at temperatures below 300 °C, SnS_2 phase became dominant at temperatures above 400 °C, but almost all impurity phases disappeared in the range of 350 °C −400 °C [71]. In alignment with these studies, a substrate temperature of 350 °C was also chosen in this study, as it yielded the dominant *π*-SnS phase in our previous works [67]. Moreover, Table 1 summarizes key parameters, including diffraction angle (*2θ*), Miller indices (*hkl*), texture coefficients (*TC*), full width at half maximum (*β*), interplanar distance (*d*), crystallite size (*D*), micro-strain (*ε*), lattice constant (*a*) and unit cell volume values (*V*), illustrating how Ag doping affects the film structure. The lattice constant (*a*) of the cubic crystal structure was calculated with Eq. (1) given below [72].

$$\frac{1}{d^2} = \frac{h^2 + k^2 + l^2}{a^2} \tag{1}$$

Here, *d* is the interplanar distance, *h*, *k* and *l* are Miller indices. The texture coefficients of the two most intense peaks were calculated using the following equation [73].

$$TC_{(hkl)} = \frac{I_{(hkl)}/I_{0_{(hkl)}}}{1/N[\sum I_{(hkl)}/I_{0_{(hkl)}}]} \tag{2}$$

Here, $I_{(hkl)}$ is the intensity value of the corresponding diffraction peak, $I_{0(hkl)}$ is the standard intensity value obtained from the JCPDS card, and *N* represents the number of diffraction peaks. The crystallite size and micro-strain values of the deposited films were calculated using

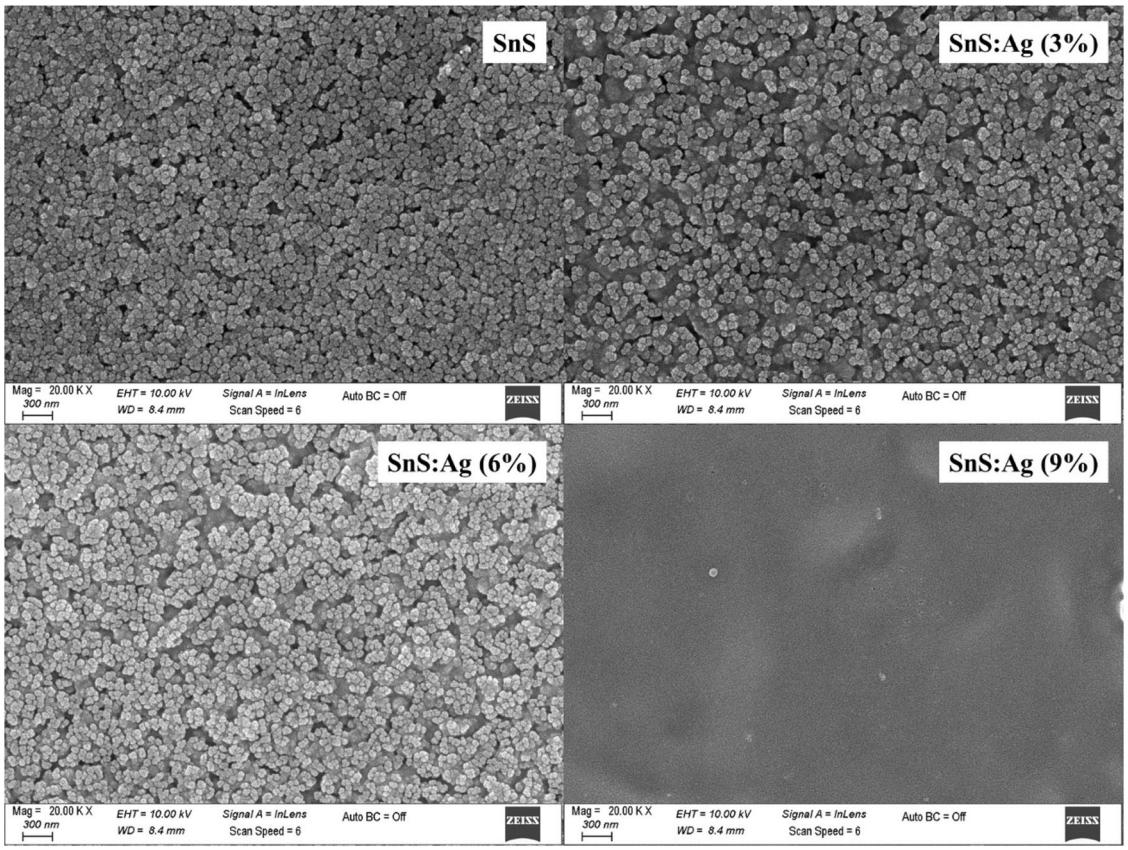

Fig. 2 ×20 K magnification SEM images of SnS:Ag (0%, 3%, 6% and 9%) thin films

Table 1 Diffraction angle (2θ), Miller indices (hkl), texture coefficients (TC), full width at half maximum (β), interplanar distance (d), crystallite size (D), micro-strain (ε), lattice constant (a) and unit cell volume values (V) obtained from structural analyses of SnS:Ag (0%, 3%, 6%, and 9%) thin films

Material	2θ (°)	(hkl)	TC	β (°)	d (Å)	D (Å)	ε×10^{-3}	a (Å)	V (Å^3)
SnS	27.07	222	0.94	0.34904	3.0990	234	6.33	10.735	1237.1
	31.27	400	1.06	0.29562	2.6912	279	4.61	10.765	1247.3
SnS:Ag (3%)	27.15	222	0.98	0.38822	3.0901	211	7.02	10.704	1226.5
	31.34	400	1.02	0.40701	2.6853	203	6.33	10.741	1239.2
SnS:Ag (6%)	27.12	222	0.95	0.3954	3.0936	207	7.15	10.717	1230.7
	31.32	400	1.05	0.40083	2.6866	206	6.24	10.746	1240.9
SnS:Ag (9%)	–	–	–	–	–	–	–	–	–

the Debye-Scherrer relation given in Eq. (3) and Eq. (4), respectively [72, 74].

$$D = \frac{K\lambda}{\beta cos\theta} \tag{3}$$

$$\varepsilon = \frac{\beta cot\theta}{4} \tag{4}$$

Here K (0.94) is the shape factor, λ is the wavelength of the x-ray used, β is the FWHM in radians, θ is the Bragg angle in radians.

When the XRD patterns given in Fig. 2b at narrowed diffraction angles are examined, shifts in the positions of the diffraction peaks of the doped films are observed. These shifts are due to the difference between the Sn^{2+} ion radius (118 pm) and the Ag^{2+} ion radius (106 pm). A successful substitution doping process should lead to a decrease in the interplanar distance (d) and a shift of the 2θ angle to higher values, as previously reported in the literature [56, 75]. The XRD patterns in Table 1 reveal a doping-dependent shift in peak positions. At 3% Ag doping, peaks shift to higher 2θ values, indicating lattice compression due to Ag^{2+} substitution at Sn^{2+} sites. At 6% Ag doping, a slight shift to lower angles is observed, suggesting that in addition to substitutional incorporation, Ag^{2+} ions also occupy interstitial sites, leading to lattice expansion. This observation is also consistent with changes in the unit cell volume values presented in Table 1, further confirming the mixed

substitutional and interstitial doping mechanism. On the other hand, it was observed that the diffraction peak intensity in the XRD patterns fluctuated depending on the Ag doping concentration. In this context, the broadening of peaks and reduction in intensity with increasing Ag doping indicate a decrease in crystallinity, suggesting the presence of enhanced lattice disorder. However, a slight narrowing and increase in the intensity of the peaks were observed with 6% Ag doping compared to the 3% doped films. Similar trends have also been reported in SnS films doped with different elements, such as Cu, In, and Ag, for both orthorhombic and cubic phases [30, 56, 75, 76]. Baby et al. [56] reported that the peak intensities decreased in SnS films doped with up to 4.7% Ag and associated this situation with the SnS structure compressing the unit cell volume and increasing the short-range order of the crystal structure. In the same study, it was observed that as the Ag doping concentration exceeded 4.7%, the XRD peak intensity increased due to the formation of new nucleation centers in the SnS structure. However, in this study, when the doping concentration was increased to 9%, no diffraction peaks could be detected in the XRD pattern. This suggests that, beyond a critical doping level (6% Ag), nucleation centers become saturated, leading to excessive lattice distortion and a breakdown of the long-range crystalline order. Consequently, the film undergoes a phase transition into an amorphous state. Additionally, the high signal-to-noise ratio in the XRD patterns suggests that potential low-density secondary phases might be present but remain undetected due to their weak diffraction signals. Reghima et al. [77] similarly reported an amorphous tendency in SnS:Ag thin films prepared by chemical bath deposition (CBD) when the silver doping concentration reached 10%. This behavior was attributed to increased stress and stacking faults caused by the higher Ag concentration, which disrupted the crystal periodicity and deteriorated the crystallinity of the films [77]. A study conducted by Bhat et al. [30], it was reported that in SnS films doped with Ag at different concentrations (0%, 5%, 10%, 15%, and 20%) by spray pyrolysis method, more than 5% Ag doping increased the formation of secondary phases such as Sn_2S_3 and SnS_2 and disrupted the π-SnS crystal structure. In the same study, a significant alteration in the triple peak structure within the 30–33° range was observed, and at 20% Ag doping, the (400) peak, characteristic of cubic SnS, disappeared entirely [30].

The *TC* values calculated in this study show that all films have (400) preferred orientation (Table 1). When the values in Table 1 are examined, it is seen that they are consistent with the peak intensity changes discussed above. In Fig. 2c, the relationship between the crystallite sizes, micro-strain, and unit cell volume, based on the (400) preferred orientation diffraction peak of the films, is presented. With increasing Ag doping, crystallite size decreases, while micro-strain increases, indicating enhanced lattice distortions. However, at 6% doping, a slight increase in crystallite size and a decrease in micro-strain suggest partial relaxation of lattice distortions, possibly due to defect rearrangement or a balance between substitutional and interstitial doping [46, 56]. As a result, the amorphization observed at 9% Ag doping is primarily due to excessive lattice strain and structural disorder, disrupting the long-range crystalline order. This phenomenon can be attributed to the increasing presence of Ag ions, which induce compressive and tensile strains within the SnS lattice. As Ag concentration rises, substitutional doping transitions into a combination of substitutional and interstitial incorporation, further increasing lattice distortions and defect formation. Studies have shown that high Ag doping concentrations in thin films often lead to amorphization due to excessive structural stress and defect accumulation [77]. The structural analyses in this study confirm that Ag doping significantly affects the crystal structure of SnS thin films, progressively reducing crystallinity, increasing micro-strain, and decreasing crystallite size, lattice constant, and unit cell volume. At high Ag doping levels, these structural transformations shift the films toward an amorphous nature, demonstrating the critical role of Ag incorporation in altering the phase stability of SnS films.

3.2 Morphological analysis

Figure 2 shows the SEM surface images of the deposited SnS films at ×20 K magnification. From these SEM images, it can be observed that the film surfaces are homogeneous, with no voids or cracks across the surface. In the SEM image of the undoped SnS film, a round-grained structure is seen, with minimal gaps between grains, indicating a dense film structure. With increasing Ag doping concentration (3% and 6%), no significant change in surface morphology is observed, but there is a noticeable increase in the gaps between grains, and a slight increase in the density of particle formations on the film surfaces. On the other hand, in the 9% Ag-doped films, the grain structure is no longer visible, and the surface appears featureless, lacking distinct grains. This observation aligns with the absence of diffraction peaks in the XRD analysis, suggesting that 9% Ag doping brings the structure closer to an amorphous character. Additionally, average grain sizes were calculated from the SEM images using ImageJ software. The average grain sizes were found to be 79 nm ± 3 nm for undoped films, 54 nm ± 6 nm for films with 3% Ag doping, and 58 nm ± 5 nm for films with 6% Ag doping. The initial reduction in average grain size observed with 3% Ag doping may be attributed to the successful substitution of Ag^{2+} cations, which have a smaller ionic radius than Sn^{2+} cations. In contrast, the slight increase in grain size

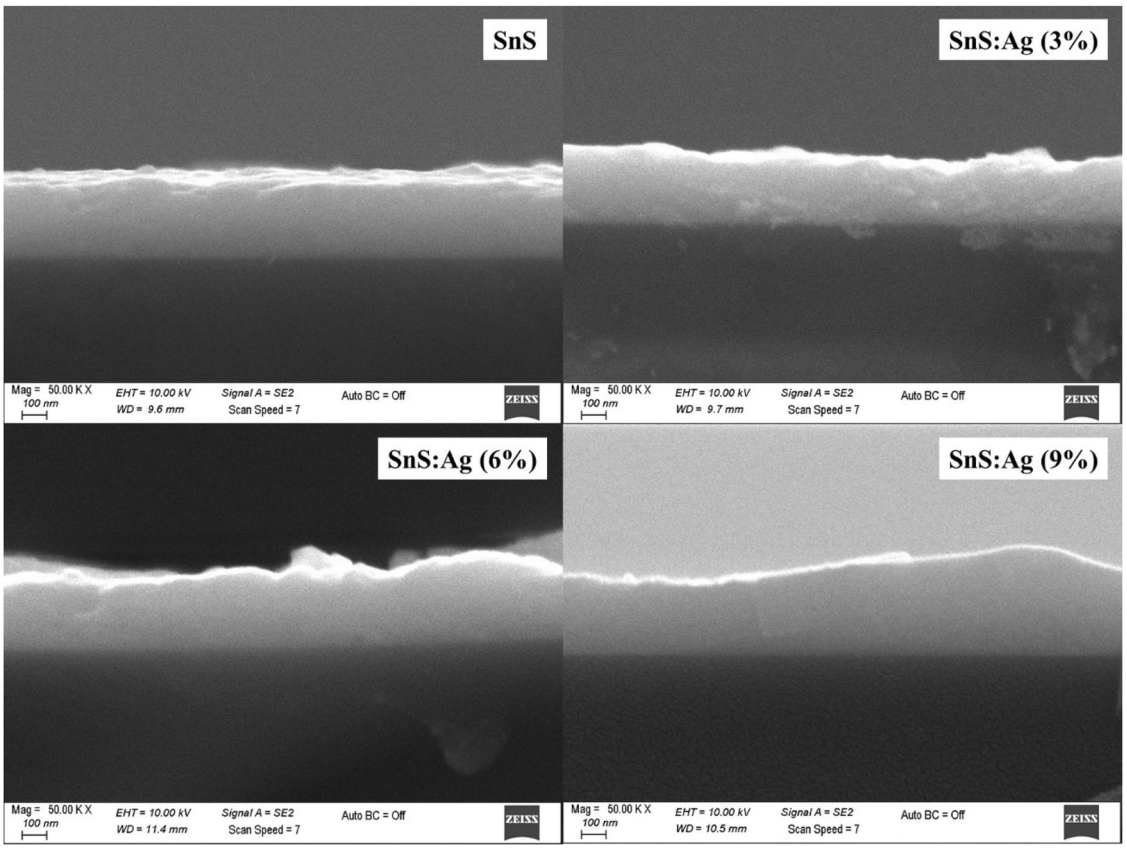

Fig. 3 ×50 K magnification cross-sectional SEM images of SnS:Ag (0%, 3%, 6% and 9%) thin films

Table 2 Average thicknesses (d), transmittance (%), absorption coefficient (α), optical band gap (E_g) derived from Tauc method and dT/dE~$h\nu$ graphs, and Urbach energy (E_u) values obtained from the optical analyses of SnS:Ag (0%, 3%, 6%, and 9%) thin films

Material	d (nm)	T (%)	α (×10^4 cm^{-1})	E_g (eV)		E_U (meV)
		400 -700 nm	400–700 nm	$(\alpha h\nu)^2$~$h\nu$	dT/d(E)~$h\nu$	
SnS	310 ± 12	11	5.21	1.84	1.81	190
SnS:Ag (3%)	256 ± 30	15	4.51	1.86	1.84	244
SnS:Ag (6%)	295 ± 25	10	5.44	1.83	1.80	245
SnS:Ag (9%)	360 ± 55	35	1.54	2.47	2.44	600

observed with 6% Ag doping could be due to the accumulation of more Ag^{2+} cations within the SnS lattice [56]. This trend is also consistent with electrical results, where increasing Ag doping led to reduced carrier mobility, likely due to enhanced grain boundary scattering. Moreover, this reduction in average grain size, along with peak broadening and decreased intensity with Ag doping, suggests an increase in structural disorder. While crystallite size estimated from XRD decreases, this does not always directly correspond to grain size observed in SEM, as additional structural defects and strain effects may also contribute to peak broadening. Similar trends have been reported in the literature for Cu-, In-, and Ag- doped SnS films [56].

Figure 3 shows the cross-sectional SEM images of the deposited SnS films at ×50 K magnification. The cross-sectional images are consistent with the surface images, showing that undoped films exhibit a dense and continuous morphology, while films with Ag doping develop a more porous and irregular cross-sectional structure. Furthermore, the thickness of each film was calculated using ImageJ software by taking measurements from ten different regions of the cross-sectional images. The average thicknesses with standard deviations were determined as follows: 310 nm ± 12 nm for undoped films, 256 nm ± 30 nm for films with 3% Ag doping, 295 nm ± 25 nm for films with 6% Ag doping, and 360 nm ± 55 nm for films with 9% Ag doping (Table 2). These values indicate that film thickness decreases slightly at lower doping concentrations, likely due to Ag incorporation modifying the nucleation rate and grain boundary formation. However, at 9% Ag doping, a

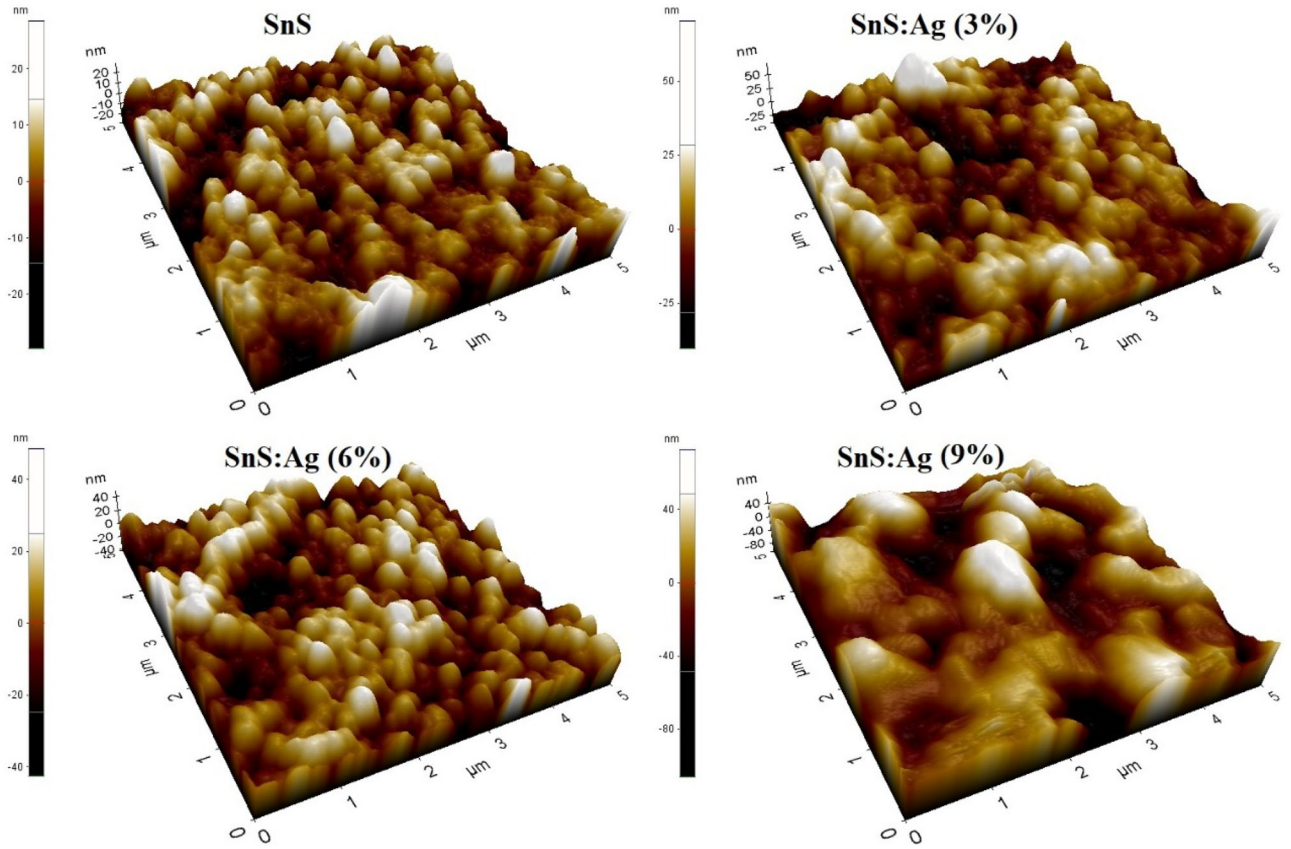

Fig. 4 AFM images of SnS:Ag (0%, 3%, 6%, and 9%) thin films

significant increase in thickness is observed, which may be attributed to Ag atom clustering and reduced atomic mobility, leading to a less compact and more porous structure. The increase in thickness at high doping concentration aligns with the XRD patterns, where lattice distortions caused by high Ag content led to amorphous characteristics. This transition to an amorphous phase likely reduces atomic mobility, disrupting the columnar growth observed in lower doping levels and promoting a more disordered, thicker film. Such structural changes, observed in both XRD and SEM images, indicate that Ag doping not only disrupts crystallinity but also modifies the growth mechanism by promoting amorphization and altering the film density and compactness.

Figure 4 presents the three-dimensional surface topographies of the deposited SnS films, as shown in the AFM images. The films generally maintain structural integrity, although surface morphology changes as Ag doping increases. The average roughness values, obtained from the AFM images for undoped, 3%, 6%, and 9% Ag-doped films, were determined as 5.8 nm, 11.3 nm, 10.1 nm, and 19.6 nm, respectively, indicating an increase in roughness with Ag doping. At the 9% doping concentration, the larger grain sizes and increased surface roughness observed in AFM image suggest that higher doping concentrations alter the surface structure of the films, resulting in a rougher and less compact surface. Although XRD analysis did not show diffraction peaks for the 9% Ag-doped SnS sample, leading it to be considered amorphous, the peaks and valleys observed in AFM images suggest the possibility of some ordered structures on the surface. This suggests that while the bulk of the film is largely amorphous, the presence of localized ordered structures may still influence charge transport and optical properties, contributing to the observed trends in resistivity and band gap widening. At 9% Ag doping, increased structural disorder and Ag-rich clustering disrupt uniform grain growth, leading to greater surface roughness and irregularities. While moderate roughness can enhance light absorption by increasing photon trapping, excessive surface irregularities can introduce additional recombination centers, which degrade photovoltaic efficiency by reducing carrier lifetimes and photocurrent. On the other hand, in comparison to similar studies, such as that by Bhat et al. [30], where roughness values ranged from 14 nm to 55 nm, the roughness values in this study remain considerably lower, even as they increase with Ag doping. In optoelectronic and photovoltaic applications, surface uniformity and controlled roughness are

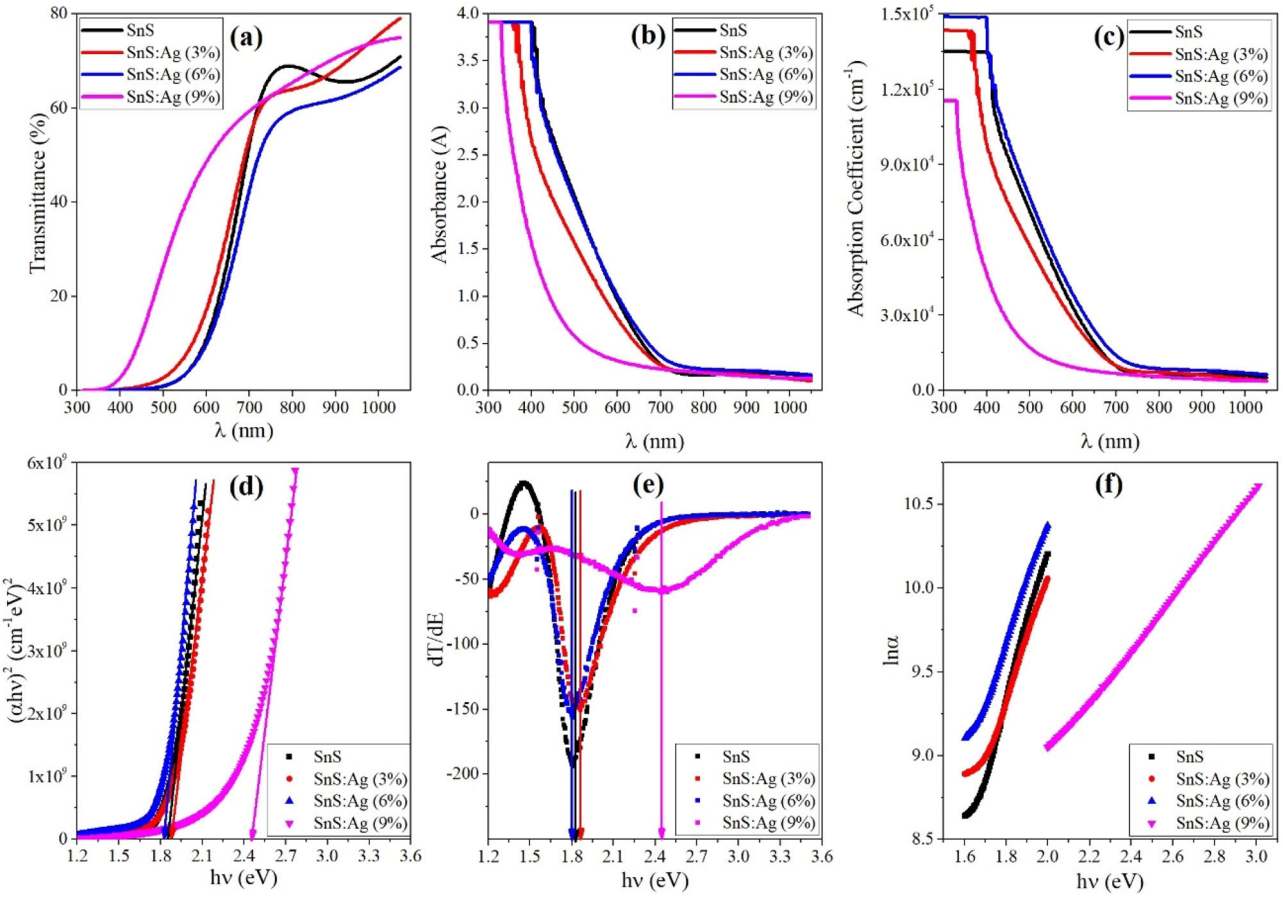

Fig. 5 **a** Transmittance spectra, (**b**) absorption spectra, (**c**) absorption coefficient spectra, (**d**) $(\alpha h\nu)^2 \sim h\nu$ graphs, (**e**) $dT/dE \sim h\nu$ graphs, and (**f**) $\ln\alpha \sim h\nu$ graphs of SnS:Ag (0%, 3%, 6%, and 9%) thin films

essential factors affecting device performance. These findings suggest that maintaining Ag doping at moderate levels ($\leq 6\%$) optimizes surface smoothness, minimizing recombination losses while preserving light absorption, making SnS films more suitable for optoelectronic applications.

3.3 Optical analysis

Figure 5a, b show the optical transmittance and absorption spectra of the deposited all films in the 300–1050 nm range. As seen from Fig. 5a, the optical transmittance of the undoped SnS thin films is 11% in the wavelength range of 400–700 nm. For SnS:Ag films, the transmittance increased to 15% at 3% Ag doping, decreased to 10% at 6% Ag doping, and significantly increased to 35% at 9% Ag doping. These values, summarized in Table 2, indicate that the optical transmittance of thin films is influenced by multiple factors, including film thickness, crystallinity, and surface homogeneity. The combined effects of these parameters, along with structural defects, doping concentration, and grain boundary scattering, collectively determine the transmittance level of the material. Similar observations have been previously reported in the literature [78, 79]. Moreover, the significant increase in transmittance observed in the 9% Ag-doped SnS films can be attributed to the amorphous structure tendency. Reghima et al. reported that 10% Ag doping in SnS films led to amorphization, reducing crystal quality and increasing transparency, likely due to lower thickness, resulting in higher transmittance than other films [77]. In this study, however, rather than thickness, the absence of grain boundaries reduces light scattering, while the structural disorder may widen the optical band gap, allowing light to pass through [80]. Furthermore, as shown in Fig. 5b, the absorption edge appears in the range of 500–700 nm, and with increasing Ag doping concentration, the absorption edge shifts toward shorter wavelengths. These spectra also indicate that the films exhibit high optical absorption, with absorption increasing as the wavelength decreases. On the other hand, Fig. 5c presents the absorption coefficient spectra calculated using the absorption data of the deposited films. The absorption coefficient (α) is given by the following equation.

$$\alpha = 2.303(A/d) \tag{5}$$

Table 3 Electrical resistivity (ρ), electrical conductivity (σ), carrier mobility (μ) and carrier concentration (N) values obtained from electrical analysis of SnS:Ag (0%, 3%, 6%, and 9%) thin films

Material	$\rho \times 10^5$ (Ωcm)	$\sigma \times 10^{-6}$ $(\Omega cm)^{-1}$	$\mu \times 10^1$ (cm^2/Vs)	$N \times 10^{12}$ (cm^{-3})
SnS	4.34	2.30	3.3	4.2
SnS:Ag (3%)	9.48	1.06	2.5	2.7
SnS:Ag (6%)	4.39	2.28	3.2	4.4
SnS:Ag (9%)	5.52	1.81	2.0	5.6

Here, A is the absorbance and d represents the film thickness [81]. As seen in Table 2, the absorption coefficient of the films ranges between $1.54 \times 10^4\,cm^{-1}$ –$5.44 \times 10^4\,cm^{-1}$, with the highest absorption coefficient observed in the SnS films doped with 6% Ag. The high absorption coefficient of SnS thin films suggests their potential use as absorber layers in TFSC applications [79, 82]. On the other hand, the band gap of the deposited films was determined by two different methods. The first of these, known as the Tauc method, was determined by using the point where the linear region of the $(\alpha h\nu)^2 \sim h\nu$ graph drawn in Fig. 5d intersects the $(h\nu)$ axis and is listed in Table 2.

$$(\alpha h\nu)^n = A(h\nu - E_g) \tag{6}$$

Here, E_g is the optical band gap, h is Planck constant, A is a constant that does not depend on energy, and ν is the frequency of light and takes the value $n = 2$ for allowed direct transitions [83]. When the values in Table 2 were examined, it was determined that the optical band gaps of undoped and 3%, 6%, and 9% Ag-doped SnS films were 1.84 eV, 1.86 eV, 1.83 eV, and 2.47 eV, respectively. The trend shows a general band gap widening with increasing Ag doping, except for 6% doping, where a slight narrowing is observed. This behavior can be explained by two competing mechanisms: (i) the Burstein-Moss effect, which occurs at high doping levels (≥ 9% Ag) due to an increase in carrier concentration, shifting the Fermi level into the conduction band [84, 85], and (ii) defect-induced localized states at 6% doping, which reduce the band gap by introducing mid-gap energy levels [77, 86]. The similarity between band gap values obtained using the Tauc method and the $dT/d(h\nu) \sim h\nu$ approach (Fig. 5e) confirms the reliability of these results, aligning well with the literature for π-SnS films doped with Ag ≤ 6% [67, 87, 88]. Additionally, structural disorder at high doping concentrations can lead to the formation of secondary phases, such as Sn_xO_y oxides, which are often amorphous or present in low concentrations, making them difficult to detect via XRD. These phases can modify the electronic structure, increasing sub-bandgap absorption while also introducing non-radiative recombination centers. Given this, highly doped SnS films (≥ 9% Ag) may be more suitable for short-wavelength photodetector applications rather than photovoltaic absorbers, which typically require a narrower band gap (1.3–1.8 eV). In addition, Urbach energy (E_U), which is a measure of the tailing at the band edges, was determined by using the slope of the linear region of the $\ln(\alpha) \sim h\nu$ graphs drawn in accordance with Eq. (7) given below in Fig. 5f and is listed in Table 2.

$$\alpha = \alpha_0 exp(h\nu/E_U) \tag{7}$$

Here α_0 is a constant [81]. The rise in Urbach energy from 190 meV (undoped) to 600 meV (9% Ag) indicates an increase in structural disorder and mid-gap defect states. While this can enhance sub-bandgap absorption for photodetectors, it may also introduce non-radiative recombination centers, reducing photovoltaic efficiency. Understanding and controlling the impact of Ag doping on the optoelectronic properties of SnS films is therefore critical for optimizing their performance in various applications.

3.4 Electrical analysis

The electrical properties of undoped and Ag-doped SnS films with different doping concentrations (3%, 6%, and 9%) were investigated using a Hall effect measurement system at room temperature, with contacts prepared in Van der Pauw geometry. The results, including resistivity (ρ), conductivity (σ), carrier mobility (μ), and carrier concentration (N), are listed in Table 3. All films exhibited p-type conductivity, which is consistent with intrinsic defects such as tin vacancies (V_{Sn}) commonly observed in SnS thin films [1, 89]. Tin vacancies create acceptor states near the valence band, enabling hole conduction and resulting in p-type behavior, as widely reported in the literature [90]. The undoped SnS film exhibits high resistivity ($4.34 \times 10^5\,\Omega cm$) and low carrier concentration ($4.2 \times 10^{12}\,cm^{-3}$), consistent with intrinsic defects like tin vacancies and possible sulfur deficiencies, which are known to dominate p-type conductivity in SnS thin films [79, 89, 91]. Previous studies have also reported comparable high resistivity values for SnS films [67, 78, 92]. Although SnS films exhibit p-type conductivity due to intrinsic defects like Sn vacancies, their low hole concentration remains a challenge for photovoltaic applications, particularly as absorber layers in TFSCs. Vidal et al. [86] suggest that increasing sulfur content during deposition can enhance hole concentration by compensating

for sulfur deficiencies. At 3% Ag doping, resistivity increases and carrier mobility decreases due to structural disorder and defect-induced scattering, limiting charge transport [85]. However, at 6% Ag doping, resistivity decreases and carrier mobility improves, suggesting Ag substitution at Sn sites, which introduces acceptor levels enhancing p-type conductivity [1]. For 9% Ag doping, the resistivity increases slightly, and mobility drops further despite a higher carrier concentration (5.6×10^{12} cm^{-3}). This behavior is attributed to amorphization, as indicated by XRD results, which creates localized states within the band gap that sustain carrier generation but increase scattering events, reducing mobility [84, 86]. Additionally, at excessive doping levels, Ag incorporation may shift from substitutional to interstitial positions within the SnS lattice, disrupting the crystal periodicity and introducing additional defect states. This transition enhances carrier scattering, further limiting mobility and increasing resistivity. Consequently, maintaining an optimal Ag doping level (≤ 6%) is crucial for achieving a balance between enhanced conductivity and minimal structural degradation.

The observed trends in electrical properties correlate with the optical characteristics of the films. The increase in Urbach energy from 190 meV to 600 meV with increasing Ag doping reflects higher structural disorder, which aligns with the reduction in carrier mobility at 9% Ag doping. Similarly, the widening of the optical band gap at higher doping concentrations may reduce the availability of thermally excited carriers, thereby contributing to the observed increase in resistivity. As previously discussed, sulfur deficiencies can also contribute to the low hole concentration, further influencing the electrical properties of the films [78, 93–95]. These results indicate a strong interdependence between the optical and electrical properties of Ag-doped SnS films, highlighting their potential as absorber layers in TFSCs. However, the relatively high resistivity and low carrier concentration observed in the present study suggest that further optimization of the Ag doping concentration and growth conditions is necessary. In particular, implementing sulfur-rich deposition conditions or post-deposition treatments such as sulfurization may effectively address sulfur deficiencies and enhance the carrier concentration.

4 Conclusion

In this study, the effects of Ag doping (3%, 6%, and 9%) on the structural, morphological, optical, and electrical properties of SnS thin films deposited via ultrasonic spray pyrolysis were investigated. XRD analysis revealed a π-SnS structure with a (400) preferred orientation for undoped and ≤6 Ag doped films, while 9% Ag doping led to amorphization. Crystallite size decreased from 279 Å (undoped) to 203 Å (3% Ag), with increasing micro-strain indicating lattice distortion. Surface analysis showed that film roughness increased from 5.8 nm to 19.6 nm with higher Ag doping, consistent with the observed structural disorder. Optical analysis demonstrated a widening of the band gap from 1.84 eV (undoped) to 2.47 eV (9% Ag), accompanied by a rise in Urbach energy from 190 meV to 600 meV, reflecting increased electronic disorder. Electrical measurements confirmed *p*-type conductivity for all films. Resistivity increased at 3% Ag doping (9.48×10^5 Ωcm) but exhibited a relatively stable trend at 6% and 9% doping concentrations, while carrier concentration rose to 5.6×10^{12} cm^{-3} at 9% doping, with mobility decreasing due to increased scattering. Based on the combined structural, optical, and electrical analyses, 6% Ag doping provides the optimal balance for thin-film solar cell applications. At this concentration, the film maintains moderate crystallinity, reasonable electrical conductivity, and an appropriate band gap (1.83 eV), avoiding the amorphization observed at 9% doping. This suggests that 6% Ag-doped SnS films are the most promising candidates for photovoltaic applications. In summary, Ag doping significantly modifies the optical and electrical behavior of SnS films, with a trade-off between structural disorder and band gap widening. These findings demonstrate the potential of Ag-doped SnS films for tunable optoelectronic applications, particularly in thin-film solar cells and photodetectors.

Data availability

No datasets were generated or analysed during the current study.

Acknowledgements This work was supported by the Canakkale Onsekiz Mart University Scientific Research Projects Committee under the project number FHD-2021-3484. We also dedicate this work to the memory of Tuncay ALDATMAZ, who was involved in the initiation of the project work but passed away.

Author contributions All authors contributed to the study's conception and design. Material preparation, data collection, and analysis were performed by I.G. and E.S. The first draft of the manuscript was written by I.G. and all authors commented on previous versions. All authors read and approved the final manuscript. Writing – original draft: I.G.; Methodology: I.G., E.S., and V.B.; Writing – review & editing, formal analysis and investigation: I.G., E.S., V.B., and A.K.; Project administration and funding acquisition: A.K.

Funding Open access funding provided by the Scientific and Technological Research Council of Türkiye (TÜBİTAK).

Competing interests The authors declare no competing interests.

References

1. Philip NM, Kumar MCS (2024) Tuning of electronic properties of co-evaporated Ag:SnS thin films for heterojunction devices. J Mater Sci Mater Electron 35:1–10. https://doi.org/10.1007/s10854-024-12078-6
2. Oni AM, Mohsin ASM, Rahman MM, Hossain Bhuian MB (2024) A comprehensive evaluation of solar cell technologies, associated loss mechanisms, and efficiency enhancement strategies for photovoltaic cells. Energy Rep. 11:3345–3366. https://doi.org/10.1016/j.egyr.2024.03.007
3. Green MA, Dunlop ED, Yoshita M, Kopidakis N, Bothe K, Siefer G, Hao X (2024) Solar cell efficiency tables (Version 63). Prog Photovolt Res Appl 32:3–13. https://doi.org/10.1002/pip.3750
4. Paul R, Shukla S, Lenka TR, Talukdar FA, Goyal V, Boukortt NEI, Menon PS (2024) Recent progress in CZTS (CuZnSn sulfide) thin-film solar cells: a review. J Mater Sci Mater Electron 35:1–21. https://doi.org/10.1007/s10854-024-11983-0
5. Gunes I, Bilgin V, Sarica E (2022) Non-stoichiometric effect and disorder in as-prepared Cu_2ZnSnS_4 films deposited at different temperatures by ultrasonic spray pyrolysis. Mater Sci Semicond Process 152:107120. https://doi.org/10.1016/j.mssp.2022.107120
6. Agrawal S, De Souza DO, Balasubramanian C, Mukherjee S (2024) Effect of secondary phases controlled by precursor composition on the efficiency of CZTS thin film solar cell. Sol Energy Mater Sol Cells 267:112719. https://doi.org/10.1016/j.solmat.2024.112719
7. Schneikart A, Schimper HJ, Klein A, Jaegermann W (2013) Efficiency limitations of thermally evaporated thin-film SnS solar cells, J Phys D Appl Phys 46. https://doi.org/10.1088/0022-3727/46/30/305109.
8. Kawano Y, Chantana J, Minemoto T (2015) Impact of growth temperature on the properties of SnS film prepared by thermal evaporation and its photovoltaic performance. Curr Appl Phys 15:897–901. https://doi.org/10.1016/j.cap.2015.03.026
9. Steinmann V, Jaramillo R, Hartman K, Chakraborty R, Brandt RE, Poindexter JR, Lee YS, Sun L, Polizzotti A, Park HH, Gordon RG, Buonassisi T (2014) 3.88% Efficient Tin Sulfide Solar Cells Using Congruent Thermal Evaporation. Adv Mater 26:7488–7492. https://doi.org/10.1002/adma.201402219
10. Sinsermsuksakul P, Sun L, Lee SW, Park HH, Kim SB, Yang C, Gordon RG (2014) Overcoming Efficiency Limitations of SnS-Based Solar Cells. Adv Energy Mater 4:1–7. https://doi.org/10.1002/aenm.201400496
11. Flores VEG, Nair MTS, Nair PK (2018) Thermal stability of "metastable" cubic tin sulfide and its relevance to applications, Semicond Sci Technol 33. https://doi.org/10.1088/1361-6641/aac524.
12. Di Mare S, Menossi D, Salavei A, Artegiani E, Piccinelli F, Kumar A, Mariotto G, Romeo A (2017) SnS thin film solar cells: Perspectives and limitations. Coatings 7:1–12. https://doi.org/10.3390/coatings7020034
13. Gohri S, Madan J, Pandey R (2024) Enhancing the efficiency of SnS-based solar cells using a GLAD technique and CZTSSe layer. Solid State Commun 377:115380. https://doi.org/10.1016/j.ssc.2023.115380
14. Cho JY, Kim SY, Nandi R, Jang J, Yun HS, Enkhbayar E, Kim JH, Lee DK, Chung CH, Kim JH, Heo J (2020) Achieving over 4% efficiency for SnS/CdS thin-film solar cells by improving the heterojunction interface quality. J Mater Chem A 8:20658–20665. https://doi.org/10.1039/d0ta06937j
15. Cheraghizade M, Jamali-Sheini F (2022) Photovoltaic behavior of SnS solar cells under temperature variations. Opt (Stuttg) 254:168635. https://doi.org/10.1016/j.ijleo.2022.168635
16. Fathy M, Elyamny S, Bishara AA, Roston GD, Kashyout AEHB (2020) SnS nanocrystalline thin films for n-CdS/p-SnS solar cell devices. J Mater Sci Mater Electron 31:18120–18134. https://doi.org/10.1007/s10854-020-04362-y
17. Sebastian S, Vinoth S, Prasad KH, Revathy MS, Gobalakrishnan S, Praseetha PK, Ganesh V, AlFaify S (2020) Quantitative analysis of Ag-doped SnS thin films for solar cell applications. Appl Phys A Mater Sci Process 126:1–12. https://doi.org/10.1007/s00339-020-03959-8
18. González-Flores VE, Mohan RN, Ballinas-Morales R, Nair MTS, Nair PK (2019) Thin film solar cells of chemically deposited SnS of cubic and orthorhombic structures. Thin Solid Films 672:62–65. https://doi.org/10.1016/j.tsf.2018.12.044
19. Gedi S, Minnam Reddy VR, Alhammadi S, Reddy Guddeti P, Kotte TRR, Park C, Kim WK (2019) Influence of deposition temperature on the efficiency of SnS solar cells. Sol Energy 184:305–314. https://doi.org/10.1016/j.solener.2019.04.010
20. Banai RE, Horn MW, Brownson JRS (2016) A review of tin (II) monosulfide and its potential as a photovoltaic absorber. Sol Energy Mater Sol Cells 150:112–129. https://doi.org/10.1016/j.solmat.2015.12.001
21. Steinmann V, Chakraborty R, Rekemeyer PH, Hartman K, Brandt RE, Polizzotti A, Yang C, Moriarty T, Gradečak S, Gordon RG, Buonassisi T (2016) A Two-Step Absorber Deposition Approach to Overcome Shunt Losses in Thin-Film Solar Cells: Using Tin Sulfide as a Proof-of-Concept Material System. ACS Appl Mater Interfaces 8:22664–22670. https://doi.org/10.1021/acsami.6b07198
22. Rabkin A, Samuha S, Abutbul RE, Ezersky V, Meshi L, Golan Y (2015) New nanocrystalline materials: A previously unknown simple cubic phase in the SnS binary system. Nano Lett 15:2174–2179. https://doi.org/10.1021/acs.nanolett.5b00209
23. Banai RE, Burton LA, Choi SG, Hofherr F, Sorgenfrei T, Walsh A, To B, Cröll A, Brownson JRS (2014) Ellipsometric characterization and density-functional theory analysis of anisotropic optical properties of single-crystal α-SnS. J Appl Phys 116:0–7. https://doi.org/10.1063/1.4886915
24. Parenteau M, Carlone C (1990) Influence of temperature and pressure on the electronic transitions in SnS and SnSe semiconductors. Phys Rev B 41:5227–5234. https://doi.org/10.1103/PhysRevB.41.5227
25. Abutbul RE, Garcia-Angelmo AR, Burshtein Z, Nair MTS, Nair PK, Golan Y (2016) Crystal structure of a large cubic tin monosulfide polymorph: An unraveled puzzle. CrystEngComm 18:5188–5194. https://doi.org/10.1039/c6ce00647g
26. Guo R, Wang X, Kuang Y, Huang B (2015) First-principles study of anisotropic thermoelectric transport properties of IV-VI semiconductor compounds SnSe and SnS. Phys Rev B - Condens Matter Mater Phys 92:1–13. https://doi.org/10.1103/PhysRevB.92.115202
27. Abutbul RE, Segev E, Zeiri L, Ezersky V, Makov G, Golan Y (2016) Synthesis and properties of nanocrystalline π-SnS-a new

cubic phase of tin sulphide. RSC Adv 6:5848–5855. https://doi.org/10.1039/c5ra23092f
28. Ahmet IY, Guc M, Sánchez Y, Neuschitzer M, Izquierdo-Roca V, Saucedo E, Johnson AL (2019) Evaluation of AA-CVD deposited phase pure polymorphs of SnS for thin films solar cells. RSC Adv 9:14899–14909. https://doi.org/10.1039/c9ra01938c
29. Cabrera-German D, García-Valenzuela JA, Cota-Leal M, Martínez-Gil M, Aceves R, Sotelo-Lerma M (2019) Detailed characterization of good-quality SnS thin films obtained by chemical solution deposition at different reaction temperatures. Mater Sci Semicond Process 89:131–142. https://doi.org/10.1016/j.mssp.2018.09.009
30. T.R Kishore, Bhat A, Pramitha K, Jeganath Y, Raviprakash (2024) The impact of silver incorporation on the structural, morphological, and optical properties of spray-pyrolyzed cubic SnS thin films. Mater Res Express 11:1–11. https://doi.org/10.1088/2053-1591/ad1b05
31. Rahman S, Sharma RK, Terrones M, Rana MM (2024) Recent Progress on Layered Sn and Pb-Based Mono Chalcogenides: Synthesis, Structure, Optical, and Thermoelectric Properties and Related Applications, Nanomaterials. 14. https://doi.org/10.3390/nano14181530.
32. Saad SKM, Umar AA, Rahman MYA, Salleh MM (2015) Porous Zn-doped TiO_2 nanowall photoanode: Effect of Zn^{2+} concentration on the dye-sensitized solar cell performance. Appl Surf Sci 353:835–842. https://doi.org/10.1016/j.apsusc.2015.06.181
33. Al-Maiyaly BKH, Muneer Sadiq D (2023) Synthesis and Characterization of SnS: 3%Bi thin Films for Photovoltaic Applications, Ibn AL-Haitham J. Pure Appl Sci 36:113–123. https://doi.org/10.30526/36.2.2930
34. Bano S, Khan MI, Albalawi H, Islam GU, Siddique M, Ahmad T, Alkhaldi H, Ben Farhat L, Ahson R, Hussain S (2022) Effect of Cd doping on the structural, optical, and photovoltaic properties of SnS films. J Mater Res Technol 19:1982–1992. https://doi.org/10.1016/j.jmrt.2022.05.137
35. Rodríguez-Castro S, Álvarez-Macías C, Salgado-Conrado L, Ruiz-Heredia IJ (2022) Experimental Analysis of SnS:Cu Thin Films Obtained by USP for their Implementation in Solar Cells Simulated by SCAPS. https://doi.org/10.9734/bpi/rdst/v3/2118b.
36. Ammar I, Gassoumi A, Turki-Kamoun N (2021) The Effect of TSC and Nickel Doping on SnS Thin Films. Silicon 13:1933–1938. https://doi.org/10.1007/s12633-020-00589-w
37. Parida A, Sahoo D, Alagarasan D, Vardhrajaperumal S, Ganesan R, Naik R (2022) Enhancing the third-order nonlinearity and crystallinity by selenium incorporation in tin sulfide films ($SnS_{1-x}Se_x$) for optoelectronic applications. Mater Adv 3:5930–5940. https://doi.org/10.1039/d2ma00485b
38. Abass KH, Adil A, Alrubaie AJ, Rabee BH, Kadim AM, Talib SH, Mohammed KA, Jassim AS (2023) Fabrication and Characterization of p-SnS/n-Si Solar Cell by Thermal Evaporation Technique and the Effect of Ag-doped on Its Efficiency. Int J Nanosci 22:572–575. https://doi.org/10.1142/S0219581X23500035
39. Kafashan H (2019) Optoelectronic properties of In-doped SnS thin fi. lms 45:334–345. https://doi.org/10.1016/j.ceramint.2018.09.172
40. Baby BH, Shajan NT, Paul Joseph D, C A F, Varghese GK, Bharathi Mohan D (2024) Phase stabilization of Fe doped SnS by solvothermal method and its structural, morphological and optoelectronic properties for photovoltaic applications. Solid State Commun 386:115525. https://doi.org/10.1016/j.ssc.2024.115525
41. Sebastian S, Kulandaisamy I, Arulanantham AMS, Valanarasu S, Kathalingam A, Shkir M, AlFaify S (2022) Enhancement in photovoltaic properties of Nd:SnS films prepared by low-cost NSP method. Rare Met 41:1661–1670. https://doi.org/10.1007/s12598-019-01295-2
42. Mahdi MS, Ahmed NM, Hmood A, Ibrahim K, Bououdina M (2019) Comprehensive photoresponse study on high performance and flexible π-SnS photodetector with near-infrared response. Mater Sci Semicond Process 100:270–274. https://doi.org/10.1016/j.mssp.2019.05.019
43. Rehman SU, Butt FK, Ul Haq B, AlFaify S, Khan WS, Li C (2018) Exploring novel phase of tin sulfide for photon/energy harvesting materials. Sol Energy 169:648–657. https://doi.org/10.1016/j.solener.2018.05.006
44. Barrios-Salgado E, Rodríguez-Guadarrama LA, Garcia-Angelmo AR, Campos Álvarez J, Nair MTS, Nair PK (2016) Large cubic tin sulfide–tin selenide thin film stacks for energy conversion. Thin Solid Films 615:415–422. https://doi.org/10.1016/j.tsf.2016.07.048
45. Norton KJ, Alam F, Lewis DJ (2021) Applied Sciences A Review of the Synthesis, Properties, and Applications of Bulk and Two-Dimensional Tin (II) Sulfide (SnS)
46. Gedi S, Reddy V, Reddy M, Ramakrishna T, Kotte R, Kim S, Jeon C (2016) Ceramics International, 42 19027–19035. https://doi.org/10.1016/j.ceramint.2016.09.059
47. Bhattacharya S, Gunda NS, Stern R, Jacobs S, Chmielowski R, Dennler G, Madsen GK (2015) Achieving optimum carrier concentrations in p-doped SnS thermoelectrics. Phys Chem Chem Phys 17:9161–9166. https://doi.org/10.1039/C4CP05991C
48. Kumar KS, Manohari AG, Dhanapandian S, Mahalingam T (2014) Physical properties of spray pyrolyzed Ag-doped SnS thin fi lms for opto-electronic applications. Mater Lett 131:167–170. https://doi.org/10.1016/j.matlet.2014.05.186
49. Tan Q, Zhao L, Li J, Wu C, Wei T (2014) Thermoelectrics with earth abundant elements: low thermal conductivity and high thermopower in. J Mater Chem A Mater Energy Sustain 2:17302–17306. https://doi.org/10.1039/C4TA04462B
50. Liu Y, Skelton JM, Xia X, Zhu Y, Lewis DJ, Freer R (2024) A combined experimental and modelling approach for the evaluation of the thermoelectric properties of Ag-doped SnS. J Mater Chem C 12:508–520. https://doi.org/10.1039/d3tc03672c
51. Lupan O, Chow L, Ono LK, Cuenya BR, Chai G, Khallaf H, Park S, Schulte A, Mary L (2010) Synthesis and Characterization of Ag- or Sb-Doped ZnO Nanorods by a Facile Hydrothermal Route. J. Phys. Chem. C 114:12401–12408. https://doi.org/10.1021/jp910263n
52. Lavanya S, Kumar TR, Juliet AV, Hakami J, Ashraf IM, Shkir M (2022) Noticeable photo-sensing properties of SnS:Cu thin films fabricated by thermal evaporation technique. Solid State Sci 128:106889. https://doi.org/10.1016/j.solidstatesciences.2022.106889
53. Zhao X, Davis LM, Lou X, Kim SB, Uličná S, Jayaraman A, Yang C, Schelhas LT, Gordon R (2021) Study of the crystal structure of SnS thin films by atomic layer deposition, AIP Adv. https://doi.org/10.1063/5.0032782.
54. Kim DG, Lee JM, Choi JH, Ahn JH (2023) Phase control of two-dimensional tin sulfide compounds deposited via atomic layer deposition. Appl Surf Sci 612:155887. https://doi.org/10.1016/j.apsusc.2022.155887
55. Chua D, Kim SB, Sinsermsuksakul P, Gordon R (2019) Atomic layer deposition of energy band tunable tin germanium oxide electron transport layer for the SnS-based solar cells with 400 mV open-circuit voltage. Appl Phys Lett. 114. https://doi.org/10.1063/1.5098766.
56. Baby BH, Bharathi Mohan D (2019) Structural, optical and electrical studies of DC-RF magnetron co-sputtered Cu, In & Ag doped SnS thin films for photovoltaic applications. Sol Energy 194:61–73. https://doi.org/10.1016/j.solener.2019.10.049
57. Arepalli VK, Kim J (2018) Effect of substrate temperature on the structural and optical properties of radio frequency sputtered tin sulfide thin films for solar cell application. Thin Solid Films 666:34–39. https://doi.org/10.1016/j.tsf.2018.09.009
58. Guc M, Andrade-Arvizu J, Ahmet IY, Oliva F, Placidi M, Alcobé X, Saucedo E, Pérez-Rodríguez A, Johnson AL, Izquierdo-Roca V (2020) Structural and vibrational properties of α- and π-SnS

polymorphs for photovoltaic applications. Acta Mater 183:1–10. https://doi.org/10.1016/j.actamat.2019.11.016
59. Khan MI, bano S, Hussain S, Alwadai N, Fatima M, Shahzad U, Yousef ES, Iqbal M (2024) Heterostructure of TiO_2 and SnS for enhancing the structural, optical and photovoltaic properties of solar cells. Opt (Stuttg) 300:171625. https://doi.org/10.1016/j.ijleo.2024.171625
60. Garmim T, Benaissa N, Louardi C, Soussi L, Mghaiouini R, Ziti A, El Jouad Z, Louardi A, El Bachiri A, Hartiti B, Monkade M (2022) Synthesis and optimization of SnS absorber layer by spin-coating process and Taguchi approach, Mater Chem Phys 292. https://doi.org/10.1016/j.matchemphys.2022.126774.
61. Kafashan H, Rabiei Baboukani A (2024) Electrochemically deposited nanostructured Cd-doped SnS thin films: Structural and optical characterizations. Ceram Int 50:5717–5727. https://doi.org/10.1016/j.ceramint.2023.11.354
62. Kumar KS, Manohari AG, Dhanapandian S, Mahalingam T (2014) Physical properties of spray pyrolyzed Ag-doped SnS thin films for opto-electronic applications. Mater Lett 131:167–170. https://doi.org/10.1016/j.matlet.2014.05.186
63. Sebastian S, Kulandaisamy I, Valanarasu S, Soundaram N, Paulraj K, Vikraman D, Kim HS (2019) Investigations on Fe doped SnS thin films by nebulizer spray pyrolysis technique for solar cell applications. J Mater Sci Mater Electron 30:8024–8034. https://doi.org/10.1007/s10854-019-01124-3
64. Gunes I, Sarica E, Bilgin V, Kucukarslan A, Ozder S (2024) Fluorine-doped tin oxide films via ultrasonic spray pyrolysis: Investigation of physical properties post-annealing and their potential for TCO applications. Mater Today Commun 41:111094. https://doi.org/10.1016/j.mtcomm.2024.111094
65. Sarica E, Ozcan HB, Gunes I, Terlemezoglu M, Akyuz I (2024) Fine-tuning SnO_2 films: Unleashing their potential through deposition temperature optimization by ultrasonic spray pyrolysis. Ceram Int 50:9270–9279. https://doi.org/10.1016/j.ceramint.2023.12.243
66. Gunes I, Sarica E, Ozcan HB, Terlemezoglu M, Akyuz I (2024) Flow rate-dependent properties of SnO_2 thin films deposited by ultrasonic spray pyrolysis. Opt Mater (Amst) 150:115189. https://doi.org/10.1016/j.optmat.2024.115189
67. Gunes I (2024) Enhancing π-SnS thin films and fabrication of p-SnS/n-Si heterostructures through flow rate control in ultrasonic spray pyrolysis for improved photovoltaic performance. Appl Phys A 130:574. https://doi.org/10.1007/s00339-024-07737-8
68. Breternitz J, Gunder R, Hempel H, Binet S, Ahmet I, Schorr S (2017) Facile Bulk Synthesis of π-Cubic SnS. Inorg Chem 56:11455–11457. https://doi.org/10.1021/acs.inorgchem.7b01623
69. Sánchez FDB, Nair MTS, Nair PK (2024) Insights to the production of SnS-cubic thin films by vacuum thermal evaporation for photovoltaics, Semicond Sci Technol 39. https://doi.org/10.1088/1361-6641/ad0f4c.
70. Polivtseva S, Acik IOja, Katerski A, Mere A, Mikli V, Krunks M (2014) Spray pyrolysis deposition of SnxSy thin films. Energy Procedia 60:156–165. https://doi.org/10.1016/j.egypro.2014.12.358
71. Sajeesh TH, Warrier AR, Kartha CS, Vijayakumar KP (2010) Optimization of parameters of chemical spray pyrolysis technique to get n and p-type layers of SnS. Thin Solid Films 518:4370–4374. https://doi.org/10.1016/j.tsf.2010.01.040
72. Cullity BD (1956) Elements of X-Ray Diffraction, Addison-Wesley Publishing Company, Inc.
73. Shinde SS, Shinde PS, Pawar SM, Moholkar AV, Bhosale CH, Rajpure KY (2008) Physical properties of transparent and conducting sprayed fluorine doped zinc oxide thin films. Solid State Sci 10:1209–1214. https://doi.org/10.1016/j.solidstatesciences.2007.11.031
74. Sarica E, Bilgin V (2017) Study of some physical properties of ultrasonically spray deposited silver doped lead sulphide thin films. Mater Sci Semicond Process 68:288–294. https://doi.org/10.1016/j.mssp.2017.06.034
75. Baby BH, Thomas AM, Amrutha EG, Bharathi Mohan D (2020) Enhancement of optoelectronic properties via substitutional doping of Cu, in and Ag in SnS nanorods for thin film photovoltaics. Sol Energy 205:446–455. https://doi.org/10.1016/j.solener.2020.05.076
76. Baby BH, Bharathi Mohan D (2018) Characterization studies of heavily doped Ag-SnS thin films prepared by magnetron co-sputtering technique. Mater Today Proc 26:108–113. https://doi.org/10.1016/j.matpr.2019.05.436
77. Reghima M, Akkari A, Guasch C, Kamoun-Turki N (2015) Structural, Optical, and Electrical Properties of SnS:Ag Thin Films. J Electron Mater 44:4392–4399. https://doi.org/10.1007/s11664-015-3971-6
78. Sarica E (2021) Investigation of spray pyrolyzed cubic structured Cu doped SnS films. Phosphorus, Sulfur Silicon Relat Elem 196:1103–1108. https://doi.org/10.1080/10426507.2021.1986498
79. Rmili A, Soussi L, Jdaa R, Garmim T, Louardi C, El Bachiri A, Louardi A, Talbi A, Nouneh K, Mabrouki M, Erguig H (2023) Cu doped SnS thin films deposited by the spray method: characterization and numerical simulation using SCAPS-1D. Opt Quantum Electron 55:1–16. https://doi.org/10.1007/s11082-023-04665-4
80. Mott NF, Davis EA (1970) Conduction in non-crystalline systems V. Conductivity, optical absorption and photoconductivity in amorphous semiconductors. Philos Mag 22:903–922. https://doi.org/10.1080/14786437008221061
81. Pankove JI (1975) Optical process in semiconductors, Dover Publications, New York
82. Gedi S, Minnam Reddy VR, Park C, Chan-Wook J (2015) R.R. Ramakrishna, Comprehensive optical studies on SnS layers synthesized by chemical bath deposition. Opt Mater (Amst) 42:468–475. https://doi.org/10.1016/j.optmat.2015.01.043
83. Tauc J, Grigorovici R, Vancu A (1966) Optical Properties and Electronic Structure of Ge. Phys Stat Sol 627:627–637
84. Saw KG, Aznan NM, Yam FK, Ng SS, Pung SY (2015) New insights on the burstein-moss shift and band gap narrowing in indium-doped zinc oxide thin films. PLoS One 10:1–17. https://doi.org/10.1371/journal.pone.0141180
85. Fadavieslam MR, Kazemi A (2017) Influence of Ag concentration on the structure, optical and electrical properties of SnS2:Ag thin films prepared by spray pyrolysis deposition. J Mater Sci Mater Electron 28:3970–3977. https://doi.org/10.1007/s10854-016-6009-9
86. Tauc J, Grigorovici R, Vancu A (1966) Optical Properties and Electronic Structure of Amorphous Germanium. Phys Status Solidi 15:627–637. https://doi.org/10.1002/pssb.19660150224
87. Khan N, Javed A, Bashir M, Bashir S (2024) Role of triethanolamine complexing agent in chemical bath deposition of tin sulfide thin films: Microstructural and optical properties. Results Opt 14:100610. https://doi.org/10.1016/j.rio.2024.100610
88. Chalapathi U, Poornaprakash B, Park SH (2016) Chemically deposited cubic SnS thin films for solar cell applications. Sol Energy 139:238–248. https://doi.org/10.1016/j.solener.2016.09.046
89. Vidal J, Lany S, Avezac M D', Zunger A, Zakutayev A, Francis J, Tate J (2012) Band-structure, optical properties, and defect physics of the photovoltaic semiconductor SnS, Appl Phys Lett 100. https://doi.org/10.1063/1.3675880
90. Duvjir G, Min T, Thi Ly T, Kim T, Duong AT, Cho S, Rhim SH, Lee J, Kim J (2017) Origin of p-type characteristics in a SnSe single crystal, Appl. Phys. Lett. 110. https://doi.org/10.1063/1.4991003
91. Ran FY, Xiao Z, Hiramatsu H, Ide K, Hosono H, Kamiya T (2016) SnS thin films prepared by H_2S-free process and its p -type thin film transistor, AIP Adv 6. https://doi.org/10.1063/1.4940931
92. Garmim T, Chahib S, Soussi L, Mghaiouini R, El Jouad Z, Louardi A, Karzazi O, El Jouad M, Hlil EK, Hartiti B, Monkade M (2020) Optical, electrical and electronic properties of SnS thin films deposited by sol gel spin coating technique for photovoltaic applications. J Mater Sci Mater Electron 31:20730–20741. https://doi.org/10.1007/s10854-020-04586-y

93. Jeganath K, Choudhari NJ, Shruthi Pai G, Rao A, Raviprakash Y (2020) Role of substrate temperature on spray pyrolysed metastable π-SnS thin films, Mater Sci Semicond Process 113. https://doi.org/10.1016/j.mssp.2020.105050
94. Gotoh T (2016) Control of carrier concentration in SnS films by annealing with S and Sn. Phys Status Solidi Appl Mater Sci 213:1869–1872. https://doi.org/10.1002/pssa.201532986
95. Minnam Reddy VR, Gedi S, Park C, Miles RW, Ramakrishna RR (2015) Development of sulphurized SnS thin film solar cells. Curr Appl Phys 15:588–598. https://doi.org/10.1016/j.cap.2015.01.022